

Applications of image analysis in concrete technology: fibres, microcracks (micro) and surface of concrete (macro)

E. RINGOT

*Laboratoire Matériaux et Durabilité des Constructions
Département de génie civil
INSA/UPS 135, avenue de Rangueil
Toulouse 31077 cedex 04 – FRANCE*

It is of first importance for research-workers, in particular in the domain of concrete and cement-based materials, to relate the properties of materials with the micro- or macro-structure. Of course, structural parameters can be obtained by physical means like X-Rays, acoustic emission, porosimetry, for instance or by mechanical tests. Nevertheless, these methods of investigation give global measurements. Contrariwise, direct methods of observation (microscopy, macroscopy) give further information and give access to more accurate and local details if needed (but in 2D only, unless tomography or stereology model are used).

The natural extension of direct observations consists in the image analysis. It undergoes a great development since more than twenty years in laboratories but it also begins to have some applications for industrial purposes.

The paper deals with three aspects of image analysis:

- the first one, a bit mathematical, will show how images of fibre reinforced mortars can be analyzed by different ways,
- the second lecture, more philosophical, will evoke some strategic questions about investigation in microcracking of concrete,
- the third will cover a technological aspect and is related to a quality requirement concerning the surface of concrete.

These topics have been covered or are actually in development in the “Laboratoire Matériaux et Durabilité des Constructions” in Toulouse, France; the name of the main contributors will appear in the head of each Section.

I. On Fibres in Concrete

K. FANUTZA, A. TOUMI, A. BASCOUL, E. RINGOT

LMDC INSA/UPS, 135 avenue de Rangueil, 31077 Toulouse, France

1. Introduction

Fibres are more and more frequently used in reinforced concrete for new buildings or for pavements reparation.

They play a major role in the mechanical behaviour of concrete: they may increase the elastic modulus, they decrease the brittleness of the material and control the opening and the development of cracks.

To improve the properties of such mixed materials so as to understand in a more precise way their mechanical behaviour, it is necessary to know how fibres are distributed and oriented in the volume.

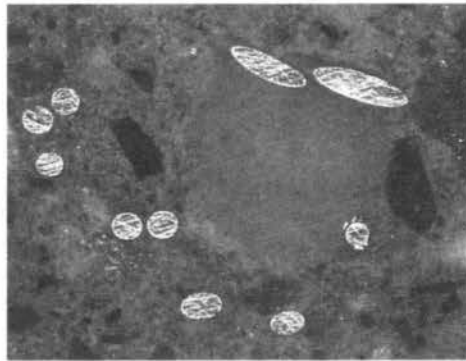


FIGURE 1. Cross section of a fibre reinforced concrete.

For example, the strength of a plane section depends not only on the number of fibres that intercept this section, but also on their leaning.

The most common fibres are cylindrical. So, in this Section, the attention will be turned to the characterisation of the numbering and the orientation of cylinders intercepted by a plane (Fig. 2). Of course, the intersection of a cylinder by a plane gives an ellipse, therefore ellipses will be at the heart of this subject.

The length of the major axis of an elliptic shape depends of the leaning of the fibre but the length of the minor axis is theoretically always equal to the diameter of the fibre. Obviously, if it is possible to find the orientation (θ) in the plane and the ratio of the two axes; consequently it is also possible to determine the leaning (α).

Note that the sign of α is undefined.

To analyse ellipse orientations, one has to proceed in two steps at least:

1. detection of the ellipses,
2. shape analysis.

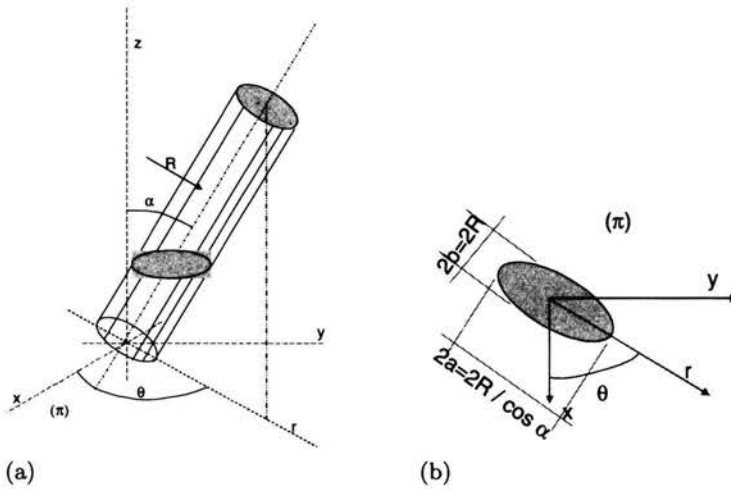


FIGURE 2. (a) Cylinder in the 3D space. (b) Cross-section of a fibre.

Images must be taken at a scale allowing for an accurate determination of the particles. The authors claim that the narrow side of each particle must count twenty pixels at least.

All the difficulty consists in finding a strong algorithm which makes possible the true shapes to be detected. It will be seen later that it can be necessary to complete this step by an enhancement process.

Once the objects of interest are extracted from the background, the shape analysis can be performed either by edge analysis or by particle analysis. At first, this implies that a particle segmentation is carried up as shown in the following Section.

2. Particle segmentation

2.1. Edge detection

The first method, edge detection needs derived images obtained by various operators such as Sobel, Prewitt, gradient or Laplacian ones (Fig. 3). In most cases, a preliminary filter is necessary to avoid artefacts.

A thresholding followed by a cleaning leads to the contour extraction (see Fig. 4).

The drawback of such a technique is that the contours can be open. Other techniques are available which leads to closed contours. Among them, let us evoke the watershed operator [S. Beucher, 1990]. This method is more complex to apply because it requires to regularise the gradient function and to mark both the objects to extract and the background.

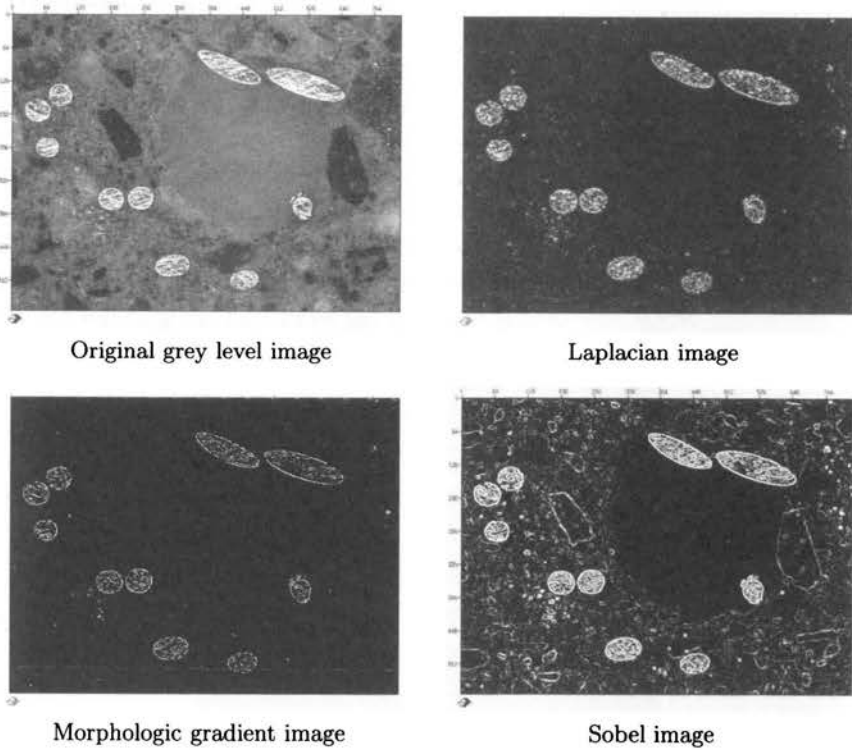


FIGURE 3. Basic edge detectors.

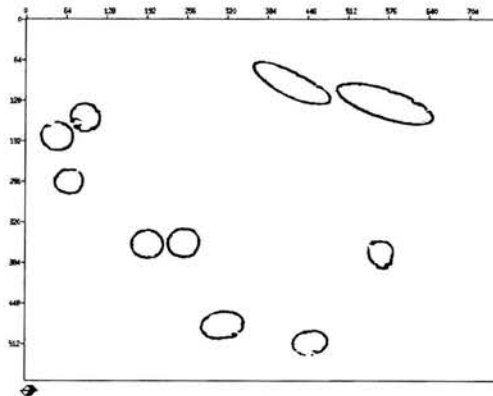


FIGURE 4. Filtered and binarized Sobel image.

2.2. Particles detection by isodata technique

Among many techniques, let us focus on the isodata algorithm [E. Diday, 1982]. In such an algorithm, each pixel is associated with a set of properties, for example the couple {grey level, local gradient} in grey level images, or the triplet {R, G, B} in the case of colour images. Other combinations of parameters are possible of course, depending on the purpose.

The pixels are projected into the space of their properties (or parameters) and they are grouped into classes (the user have to choose the desired number of classes). In each class, the parameter values are similar and the pixels are found to be distributed around a 'kernel' (Fig. 5).

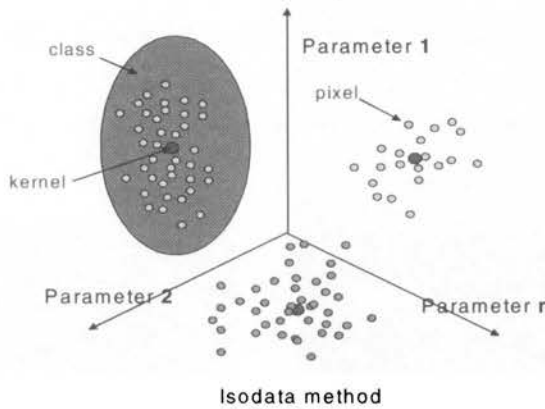


FIGURE 5. Parameter space representation of pixels.

Let us define:

- N – the number of classes,
- P – the number of parameters,
- g_i – the kernel of the class C_i .

The inertia of the class C_i is calculated by

$$W_i = \sum_{x \in C_i} d^2(x, g_i),$$

where d is the Euclidian distance in the parameter-space IR^P of P dimensions.

So, the total inertia is:

$$W = \sum_{i=1}^N W_i.$$

Among all the possible sets of partitions, the optimal one minimises W . This problem of minimisation can be solved in an iterative way. For this purpose we need two functions:

1. One function h for the representation, which determines the kernel for each class: in fact, g_i is often the gravity centre of the class C_i :

$$h : \{C\} \rightarrow \{g\} : \bar{g}_i = \frac{1}{N_i} \sum_{x \in C_i} \bar{x}_i \quad (\text{there are } P \text{ components}).$$

2. One function f for the affectation which determines the unique partition associated with the kernels g_i . The class C_i is formed by all the pixels that are nearer g_i than any else kernel:

$$f : \{g\} \rightarrow \{C\} : C_i = \{x \in \text{Image}, \forall j \neq i, d(x, g_i) < d(x, g_j)\}.$$

The initialisation of the algorithm is made by an initial evaluation of the kernels (or by randomisation). The algorithm is given in Table 1. At each

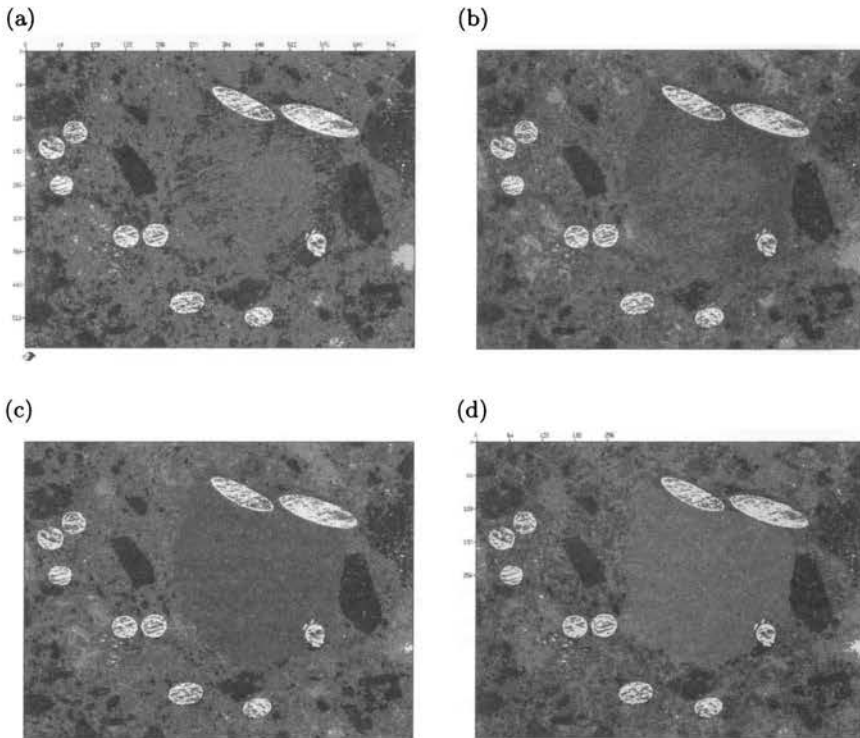


FIGURE 6. Starting (a), intermediate (b,c), and final (d) stages of an isodata process.

step, it is possible to replace each pixel by the kernel of its class to visualise the intermediate images (see Fig. 6, from (a) to (d)).

TABLE 1. Isodata algorithm.

<ol style="list-style-type: none"> 1. Initialize the N kernels $\{g^0\}$. 2. Build the set of classes $\{C^{k+1}\} = f(g^k)$ around the kernels. 3. Build the new set of kernels: $\{g^{k+1}\} = h(C^{k+1})$. 4. Determine the total inertia $W^{k+1} = W(C^{k+1}, g^{k+1})$. 5. If $\{g^{k+1}\} \equiv \{g^k\}$ then stop (stationarity) else go to step 2.

Then the class(es) concerning the particles is (are) extracted, filtered and closed (see Fig. 7).

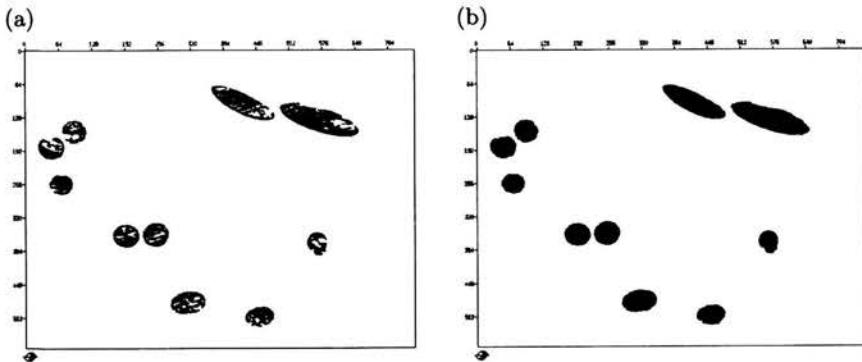


FIGURE 7. Class corresponding to fibres (a), and after filling and morphologic filtering (b).

2.3. Contour enhancement with snakes

The enhancement of the edges detected by the procedure of segmentation is useful to obtain more convex shapes as expected by the researcher. It can be also used to close edges, if necessary.

Kass [M. Kass, 1987] has proposed a model called “active contour” or “snakes” with the aim of forming a contour the form of which is influenced both by internal and external constraints.

A snake is a contour defined by a set of control points. The contour passes through these points. In fact, it is not necessary closed but here only the case of closed snakes will be evoked.

The position and the shape of the snake must comply with intrinsic properties that are imposed (smoothness or elasticity for example) and image-

related properties that are desired (for instance, accordance with the gradient of the image $g(x, y)$).

Based on these properties, an energy functional, depending on the contour $\vec{v}(s)$ is defined:

$$E_{\text{snake}} = \oint e_{\text{snake}}(\vec{v}(s)) ds, \quad (2.1)$$

where E_{snake} represents the global energy and e_{snake} the local one which can be decomposed into two terms of energy $e_{\text{snake}} = e_{\text{int}} + e_{\text{ext}}$, given by

$$e_{\text{int}} = \frac{1}{2} \left(\alpha(s) |v_s(s)|^2 + \beta(s) |v_{ss}(s)|^2 \right), \quad (2.2)$$

$$e_{\text{ext}} = |\text{grad}(g)| = \sqrt{\left(\frac{\partial g}{\partial x}\right)^2 + \left(\frac{\partial g}{\partial y}\right)^2}. \quad (2.3)$$

In these expressions, $v_s(s)$ is a first order term which increases when the distance between two control points becomes large and $\alpha(s)$ represents the local elasticity.

$v_{ss}(s)$ is a second order term which increases with the curvature of the contour and $\beta(s)$ represents the binding factor. The relative weights of α and β depend on the chosen influence of the elasticity on the curvature. Concerning the enhancement, it is pertinent to give a large value to β so that the minimization of E_{snake} occurs when the contour is very smooth. Contrariwise, a small value for β (i.e. null) would enable sharp corners to appear in the contour.

Theoretically, the problem must be solved by a variational calculus, but it can be shown [A. Amini, 1988] that in a discrete context, an iterative process called 'dynamic programming' can be successfully applied.

The discrete formula for the snake energy becomes:

$$E_{\text{snake}} = \sum \alpha_i v_s^i + \beta_i v_{ss}^i + e_{\text{ext}}^i. \quad (2.4)$$

D.J. Williams and M. Shah [D.J. Williams, 1991] have proposed the following estimators for each term:

1. The first term, also called 'continuity term', has not the usual expression $v_s^i = |\vec{v}_i - \vec{v}_{i-1}|$ because it would contribute to minimize the distance between two consecutive points, thus leading to a shrinking of the snake. It seems more pertinent to encourage even spacing to reflect the desired regularity of the contour. Thus the final expression uses the difference between the mean distance \bar{d} and the local distance, so that, the continuity term becomes $v_s^i = |\vec{v}_i - \vec{v}_{i-1}| - \bar{d}$.

2. The second term, or 'curvature term', is estimated by: $v_{ss}^i = \left| \frac{d^2 \vec{v}_i}{ds^2} \right| \approx |\vec{v}_{i-1} - 2\vec{v}_i + \vec{v}_{i+1}|$. Here it is assumed that the points are spaced at unit interval, or at least that they are evenly spaced as they are supposed to be, according to the previous 'continuity term'.
3. The third term is the gradient magnitude derived from Sobel's or Prewitt's transformation applied to the original (filtered) image.

Finally the algorithm is almost simple, see Table 2 and Fig. 8.

TABLE 2. Snake algorithm.

```

do
  flag down
  E_min = BIG_VALUE
  for each control point i
    for each neighbour j
      E_j = alpha * v_s^j + beta * v_ss^j + gamma * e_ext^j
      if (E_j < E_min) then
        E_min = E_j
        j_min = j
      end if
    end for j
    move point i to location j_min
    if (j_min not current location) then
      flag up
    end if
  end for i
until flag
    
```

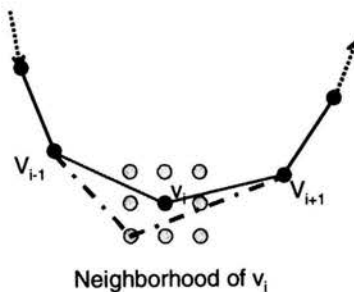


FIGURE 8. Part of an active contour.

The algorithm has been implemented to enhance one contour at a time. Images presented in Fig. 9 show an example of the successive steps of such a process. The control points are taken from the initial edge. Note that it

cannot be asserted that the final shape, although smoother and more convex than the initial one, is a perfect ellipse.

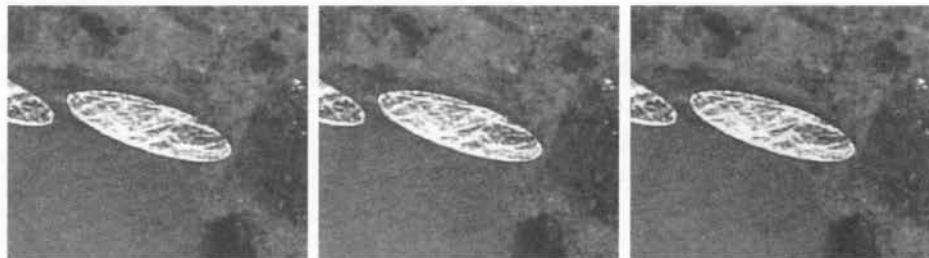


FIGURE 9. Example of a snake process.

3. Shape analysis

3.1. Diametrical variation of elliptic shapes

This Section applies to particle after its detection.

It is necessary to introduce the concept of diametrical variation of a particle. Let us consider a network of parallel oriented straight lines drawn in the plane. These lines go across a particle. If the distance between two lines is denoted by $dD_2(\alpha)$, the diametrical variation in the direction α is given by:

$$D_2(\alpha) = \oint_{\partial L} \eta_\alpha(P) dD_2, \quad (3.1)$$

where the function $\eta_\alpha(P)$ indicates if a line gets out of the particle at point P on the edge (∂L) (value 1) or not (value 0).

Note that, in the case of non-convex particle, the diametrical variation is different from Ferret's diameter in the same direction.

Of course, the diametrical variation $D_2(\alpha)$ depends on the orientation α of the lines.

For instance, among other applications of $D_2(\alpha)$, the mathematician Cauchy showed that the perimeter of a particle is given by:

$$p = \int_{\alpha=0}^{\alpha=\pi} D_2(\alpha) d\alpha. \quad (3.2)$$

In the case of image analysis, and particularly in the case of square lattice images, only some directions are available because of the discretisation of the

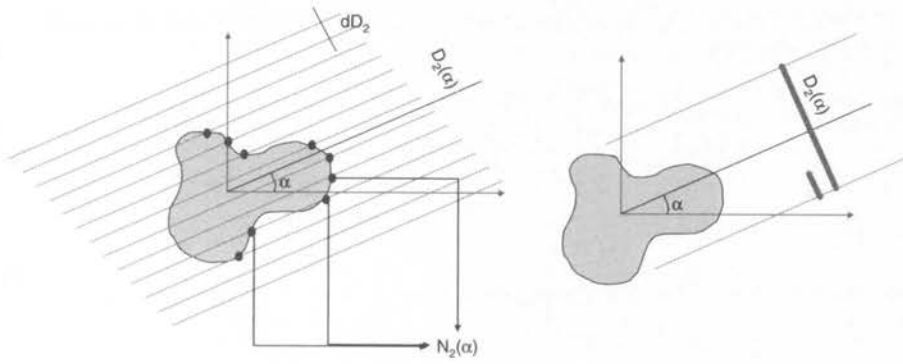


FIGURE 10. Diametrical variation of a particle.

space. The expression $D_2(\alpha) = \oint_{\partial L} \eta_\alpha(P) dD_2$ must be replaced by a digitized one:

$$D_2(\alpha) = N_2(\alpha) dD_2, \tag{3.3}$$

where $N_2(\alpha)$ is the number of lines leaving the particles. In fact, no line is drawn on the image, but $N_2(\alpha)$ is obtained from the detection of particular configurations of pixels.

In a square lattice, height directions can be examined, as shown in Table 3.

Generally the width to height ratio of a pixel is equal to the unit because square pixels are generated.

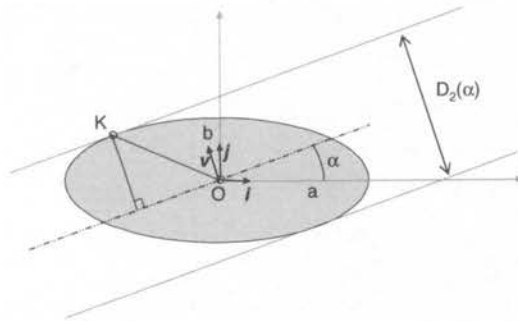
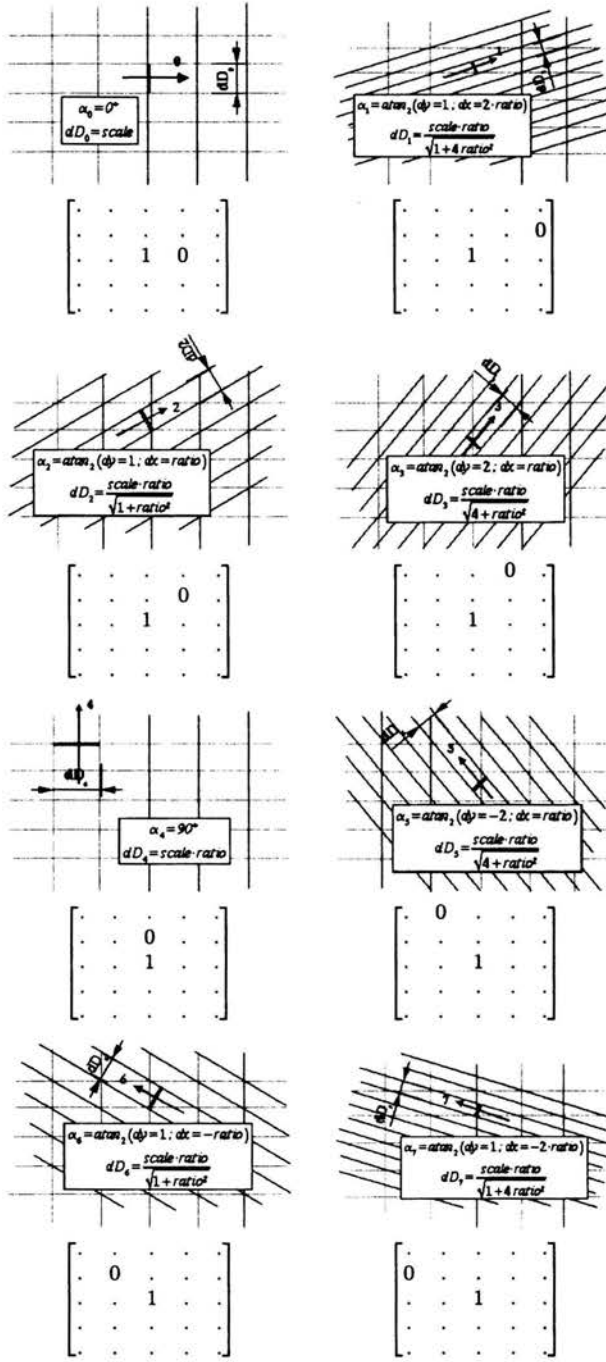


FIGURE 11. Non-oblique (or “parallel”) ellipse.

The equation of the ellipse in its own system of axes is:

$$\frac{x^2}{a^2} + \frac{y^2}{b^2} = 1. \tag{3.4}$$

TABLE 3. The height discrete directions of a rectangular lattice and their corresponding neighbours.



An ellipse is convex and its diametrical variation is equal to the projection of its edge in the direction perpendicular to α .

Let K be the point belonging to the ellipse and the tangent whose leaning is α . The diametrical projection is twice as long as the projection of \overrightarrow{OK} : $D_2(\alpha) = 2|\overrightarrow{OK} \cdot \vec{v}|$, where $\vec{v} = -\sin(\alpha)\vec{i} + \cos(\alpha)\vec{j}$.

Since $\overrightarrow{OK} = x\vec{i} + y\vec{j}$, therefore: $D_2(\alpha) = 2|-x \sin(\alpha) + y \cos(\alpha)|$.

The coordinates of K comply with Eq. (3.4) and the local tangent can be derived from the differential:

$$\frac{2x \, dx}{a^2} + \frac{2y \, dy}{b^2} = 0. \tag{3.5}$$

Consequently we get:

$$\tan \alpha = \frac{dy}{dx} = -\frac{b^2 \, x}{a^2 \, y}.$$

Finally, solving the system:

$$\begin{cases} \frac{x^2}{a^2} + \frac{y^2}{b^2} = 1, \\ \tan \alpha = \frac{dy}{dx} = -\frac{b^2 \, x}{a^2 \, y}, \\ D_2(\alpha) = 2|-x \sin(\alpha) + y \cos(\alpha)|, \end{cases} \tag{3.6}$$

the following expression for the diametrical variation is obtained:

$$D_2(\alpha) = 2\sqrt{a^2 \sin^2(\alpha) + b^2 \cos^2(\alpha)}. \tag{3.7}$$

In the case of an oblique ellipse, with an angle of obliquity equal to φ (Fig. 12), the diametrical variation becomes:

$$D_2(\alpha) = 2\sqrt{a^2 \sin^2(\alpha - \varphi) + b^2 \cos^2(\alpha - \varphi)}. \tag{3.8}$$

It depends on the three parameters a , b , φ .

Now, assuming that the eight diametrical variations D_i , $i = 0, \dots, 7$, of an elliptic-shaped particle are known, the question is to find the parameters characterising the investigated ellipse.

Five parameters are necessary to entirely determine an ellipse but if its centre is not concerned, only three of them are enough to define its shape: the two half-lengths of the axes and the orientation.

Here, the least-square method can be proposed to deduce those three parameters from the eight data. Furthermore, the result must be tolerant to some incertitude in the initial data.

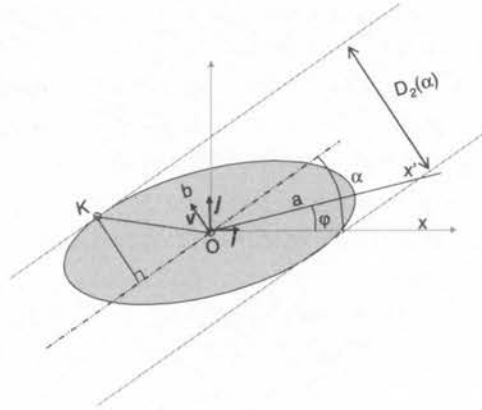


FIGURE 12. Oblique ellipse.

The square of the theoretical diametrical variation is:

$$\begin{aligned} [D_2(\alpha)]^2 &= 4 (a^2 \sin^2 (\alpha - \varphi) + b^2 \cos^2 (\alpha - \varphi)) \\ &= 2 \left[(a^2 + b^2) - (a^2 - b^2) \cos (2(\alpha - \varphi)) \right]. \end{aligned}$$

This relation can be written as:

$$\begin{aligned} [D_2(\alpha)]^2 &= u - v \cos (2(\alpha - \varphi)), \\ \text{with: } u &= 2(a^2 + b^2) \quad \text{and} \quad v = 2(a^2 - b^2). \end{aligned} \tag{3.9}$$

The square difference between the theoretical and the eight effective measures to be minimised is:

$$\Delta = \sum_{i=0}^{i=7} (u - v \cos 2(\alpha_i - \varphi) - D_i^2)^2, \tag{3.10}$$

where u , v , and φ must comply with the following three derivatives:

$$\begin{cases} \frac{\partial \Delta}{\partial u} = 0, \\ \frac{\partial \Delta}{\partial v} = 0, \\ \frac{\partial \Delta}{\partial \varphi} = 0. \end{cases} \tag{3.11}$$

Hence:

$$\begin{cases} \sum_i (u - v \cos 2(\alpha_i - \varphi) - D_i^2) = 0, \\ \sum_i (u - v \cos 2(\alpha_i - \varphi) - D_i^2) \cos 2(\alpha_i - \varphi) = 0, \\ \sum_i (u - v \cos 2(\alpha_i - \varphi) - D_i^2) v \sin 2(\alpha_i - \varphi) = 0. \end{cases}$$

We set $C_i = \cos 2(\alpha_i - \varphi)$, $S_i = \sin 2(\alpha_i - \varphi)$,

$$\begin{cases} 8u - v \sum_i C_i = \sum_i D_i^2, \\ u \sum_i C_i - v \sum_i C_i^2 = \sum_i D_i^2 C_i, \\ u \sum_i S_i - v \sum_i S_i C_i = \sum_i D_i^2 S_i. \end{cases}$$

Eliminating u and v from this system, it is found that φ must comply with the following equation:

$$\begin{aligned} & \left[\frac{1}{8} \left(\sum_i C_i \right)^2 - \sum_i C_i^2 \right] \left[\sum_i D_i^2 S_i - \frac{1}{8} \sum_i S_i \sum_i D_i^2 \right] \\ & - \left[\frac{1}{8} \sum_i C_i \sum_i S_i - \sum_i C_i S_i \right] \left[\sum_i D_i^2 C_i - \frac{1}{8} \sum_i C_i \sum_i D_i^2 \right] = 0. \end{aligned} \quad (3.12)$$

Solving Eq. (3.12) (for example iteratively), φ is then found. Then u and v are obtained from the following relations:

$$v = \frac{\sum_i D_i^2 C_i - \frac{1}{8} \sum_i C_i \sum_i D_i^2}{\frac{1}{8} \left(\sum_i C_i \right)^2 - \sum_i C_i^2}, \quad (3.13)$$

$$u = \frac{\sum_i D_i^2 + v \sum_i C_i}{8}. \quad (3.14)$$

Once u and v are known, it is easy to get a and b . Note that if u is found to be lower than v , $\frac{\pi}{2}$ must be added to φ as well as u and v have to be permuted.

The advantage of this technique is that it is not necessary to extract each point of the edge. The disadvantage is that it cannot yield more than eight data for the calculation of the parameters. The centres of the ellipses are assumed to be the geodesic centres of each particle.

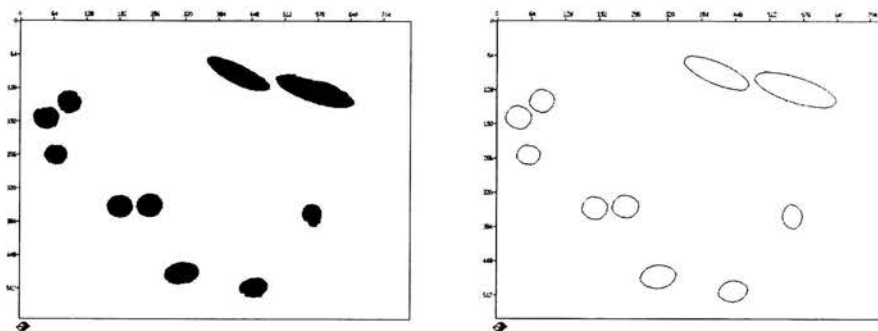


FIGURE 13. Initial and final ellipses.

The ellipses on the right image of Fig. 13 are drawn by using Bresenham's algorithm [J.E. Bresenham, 1977/1985] as described in [D. Eberly, 2000]. The quantitative results are summarized in Table 4.

TABLE 4. Fibre analysis (example).

There are 10 fibres:					
No.	centre location (in pixel)		axe lengths (in pixel)		orientation (in degree)
0	412	96	66	21	155
1	561	127	80	25	163
2	84	149	24	22	7
3	40	180	25	22	171
4	59	250	23	19	178
5	242	346	26	22	1
6	184	349	25	22	179
7	556	364	23	19	102
8	304	477	34	22	9
9	445	504	28	20	9

3.2. Specific Hough Transform for ellipses detection

The Hough Transform [P.V. Hough, 1959] was originally imagined to isolate straight lines in images. Next, it was extensively developed and applied in other situations, in particular for circles and ellipses detection.

The Hough Transform (HT) requires the desired features to be specified in a parametric form.

3.2.1. Straight line HT. The initial binary image is formed by a set of pixels derived from an edge detector. The basic idea underlying Hough Transformation is that each pixel belongs to a physical line.

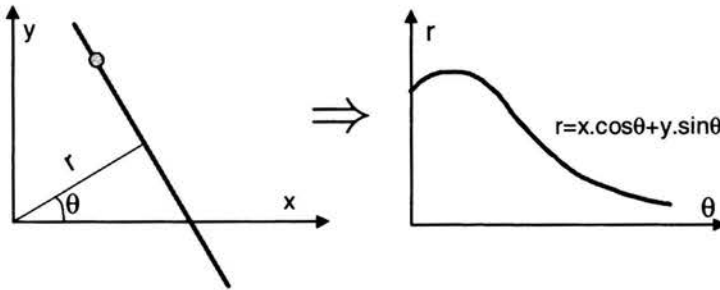
A parametric representation of a straight line can be expressed by:

$$x \cos(\theta) + y \sin(\theta) = r,$$

where r is the distance between the line and the origin $O(0,0)$ of the image and θ is the orientation of the line (Fig. 14(a)).

To each pixel $\{x, y\}$, corresponds a sinusoidal curve in the space of the two parameters $\{r, \theta\}$ describing all the lines that pass through this pixel (Fig. 14(b)). When several pixels belong to the same straight line (Fig. 14(c)), each Hough Transform goes through the same accumulation point (Fig. 14(d)).

(a) Initial pixel in the image space. (b) Hough Transform in parameter space.



(c) Three pixels on the same line. (d) Accumulation in the parameter space.

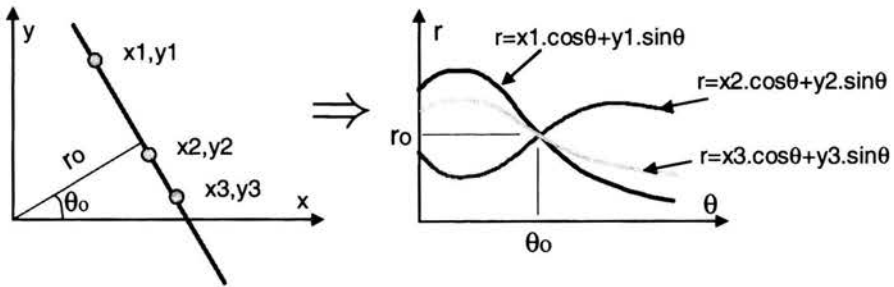


FIGURE 14. Straight line and its Hough Transformation.

In practice the transformation is implemented by discretising the Hough parameter space into finite intervals (for example from half degree to half degree for the angles and from one pixel to one pixel for the distances).

In the parameter space, a value is incremented every time a curve goes through a point so that a matrix of accumulator cells is built. Resulting peaks in the accumulator array represent strong evidence that a corresponding straight line exists in the image. An example is given in Fig. 15. The bright intersection points characterise the straight lines of the original image. They are extracted by detecting the maxima of grey levels in the parameter space represented by an image in Fig. 15(b).

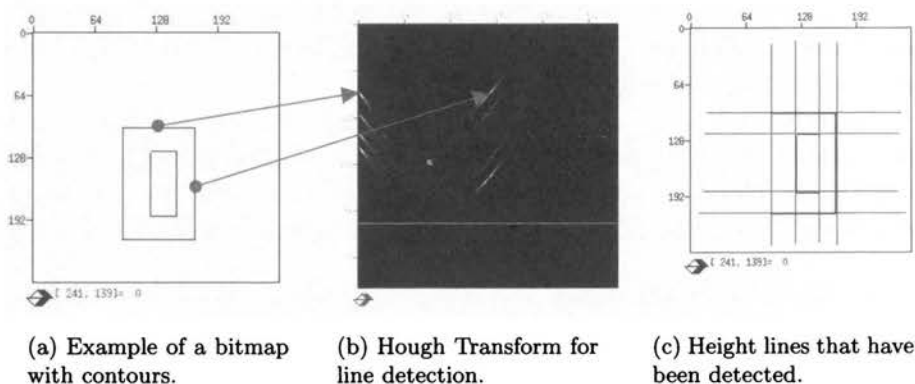


FIGURE 15. Schematic binary image and its Hough Transform.

3.2.2. Circle Hough Transformation. The same procedure can be used in the case of circle detection. For instance, the parametric equation takes the form: $(x - x_C)^2 + (y - y_C)^2 = r^2$, so that three parameters are needed (y_C and x_C are the co-ordinates of the centre of the circle). Obviously, the computational complexity increases with the number of parameters. Finally, the basic HT described above is only practical for simple curves. For more complex shapes, another algorithm is required as it is shown for the ellipses.

3.2.3. Randomized Hough Transformation of ellipse. The problem of recognizing ellipses of any size, position and orientation has been studied by McLaughlin [R.A. McLaughlin, 1997].

The parametric equation of the ellipse of Fig. 16 is given by:

$$\alpha(x - x_C)^2 + 2\beta(x - x_C)(y - y_C) + \gamma(y - y_C)^2 = 1, \quad (3.15)$$

which is equivalent to:

$$\left[\frac{(x - x_C) \cos \varphi + (y - y_C) \sin \varphi}{a} \right]^2 + \left[\frac{-(x - x_C) \sin \varphi + (y - y_C) \cos \varphi}{b} \right]^2 = 1.$$

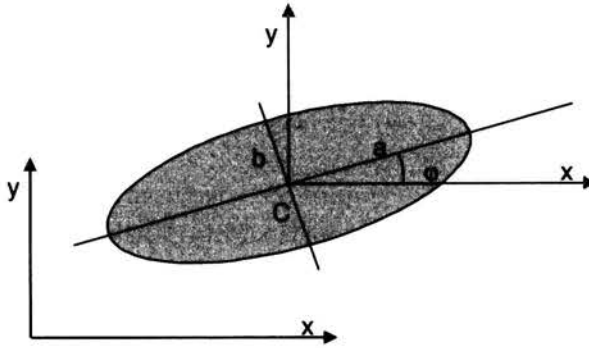


FIGURE 16. Oblique ellipse.

Such an equation involves five parameters so that the basic HT algorithm is not applicable.

The algorithm proposed by McLaughlin is a stochastic process, the so-called Randomized Hough Transform (RHT).

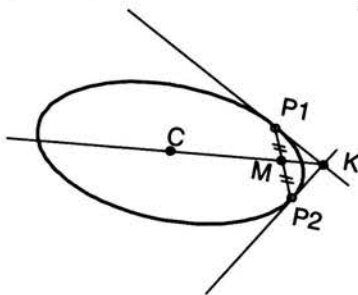
Once again, the original image must be pre-processed with an edge detection operator (Sobel, Canny [J.F. Canny, 1986], etc.) so that a binary image is available.

The following geometric properties of the ellipse are exploited (see Fig. 17) [W. Wu, 1993]:

- tangent property,
- centre.

Given two arbitrary tangents to the ellipse at points P_1 and P_2 and K their point of intersection (Fig. 17(a)), the line going from the centre of the ellipse to the point K goes through the middle M of the segment $[P_1P_2]$.

(a) Tangent property.



(b) Finding the centre of an ellipse.

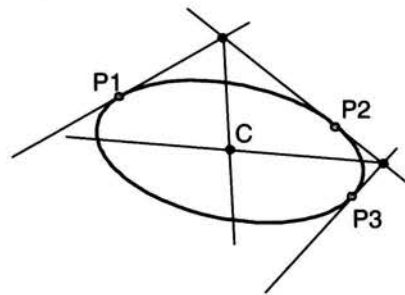


FIGURE 17. Geometric properties of the ellipse.

Inversely, from three points P_1, P_2, P_3 , it is possible to find the centre (Fig. 17(b)).

The algorithm proposed by McLaughlin was described and implemented by Schuler on a Matlab platform [A. Schuler, 2001]. The successive steps are as follows:

1. Take any 3 points belonging to the edge from the binary image.
2. Estimate the location of the centre C of the ellipse. If the centre cannot be found (because the three points do not belong to the same elliptic edge), go back to (1). The tangent at points P_1, P_2, P_3 are estimated by a least square method applied to neighbourhood of each point.

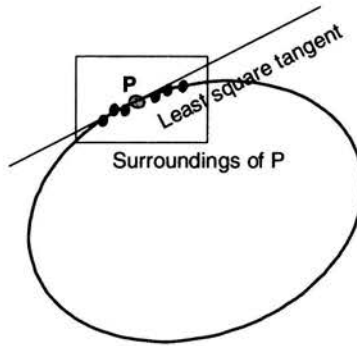


FIGURE 18. Finding a local tangent.

3. Translate the origin to the centre by modifying the coordinates of the three points. So that the equation of the ellipse simplifies to:

$$ax^2 + 2bxy + cy^2 = 1. \quad (3.16)$$

4. Compute the parameters α, β , and γ by solving the system of equations (P_1, P_2 and P_3 belong to the same edge):

$$\begin{bmatrix} x_1^2 & 2x_1y_1 & y_1^2 \\ x_2^2 & 2x_2y_2 & y_2^2 \\ x_3^2 & 2x_3y_3 & y_3^2 \end{bmatrix} \begin{bmatrix} \alpha \\ \beta \\ \gamma \end{bmatrix} = \begin{bmatrix} 1 \\ 1 \\ 1 \end{bmatrix}. \quad (3.17)$$

Check the inequality $\alpha\beta - \gamma^2 > 0$ which is always true for an ellipse. If false, go back to (1).

5. Compute the geometric parameters a, b , and θ (x_C and y_C are already known).

6. Search the parameters $\{x_C, y_C, a, b, \theta\}$ among the list of already found parameter sets. If there is a parameter set whose values match the ones newly found (in the limits of the tolerance), increase the count of this parameter set (accumulation). Each parameter set possesses a count value which tells how many times these parameters have been found. If the new parameters do not match any parameters in the list, simply add them to the list and initialise their count to 1.
7. After a specified amount of parameter sets have been found, analyse the list and keep the parameters for which the count is high (or above some threshold).

The advantage of this algorithm is that it can detect several edges at a time. Results will be discussed later on.

3.3. Straightforward computation by the least square method

Among all other methods, ellipse recognition can be performed by fitting a primitive model to the image data. The typical way for that consists in detecting the edges, then isolating each of them and finally fitting them to an elliptic shape.

Recent works relate to the problem of fitting [W. Gander, 1994], [P.L. Rosin, 1993]. Most of the methods are iterative, fitting data to general conic and rejecting non elliptic shapes.

Most of these techniques work well when data belong precisely to an elliptic arc; contrariwise most of them suffer of less ideal condition such as noise, non-strictly elliptic data or moderate occlusion [P.D. Sampson, 1982], [K. Kanatani, 1994], [J. Porril, 1990].

Let us enumerate the optimal conditions for an almost good ellipse-fitting method [A. Fitzgibbon, 1999]:

- ellipse-specificity,
- inclusion and noise tolerance,
- invariance to linear transformation of the data,
- computational efficiency.

Least squares methods lead to finding the set of parameters that minimise the distance measured between the N data points and the ellipse [R. Haralick, 1992].

Let an implicit second order polynomial be the equation of a conic curve:

$$f(\vec{a}, \vec{x}) = ax^2 + bxy + cy^2 + dx + ey + f = 0, \quad (3.18)$$

where $\vec{a} = [a, b, c, d, e, f]^T$ and $\vec{x} = [x^2, xy, y^2, x, y, 1]^T$. $f(\vec{a}, \vec{x}_i)$ is the algebraic distance between the point (x, y) and the conic $f(\vec{a}, \vec{x}) = 0$. Fitting the

data to a general conic curve leads to the minimisation of the sum of the squared distances:

$$\delta(\vec{a}) = \sum_{i=1}^n f^2(\vec{a}, \vec{x}_i). \quad (3.19)$$

The vector \vec{a} must be constrained in order to eliminate the multiples of solution so as the trivial solution we have $\vec{a} = \vec{0}$. These constraints are either linear in the form $\vec{C} \cdot \vec{a} = 1$ [W. Gander, 1994], [P.L. Rosin, 1993], or in the form $\vec{a}^T C \cdot \vec{a} = 1$ [G. Taubin, 1991]. In the last expression, C represents a 6×6 constraint matrix.

When a quadratic constraint is imposed on the parameters \vec{a} , Bookstein showed that the minimisation of $\delta(\vec{a})$ leads to a generalised eigenvalue problem:

$$D^T D \vec{a} = \lambda C \vec{a}. \quad (3.20)$$

Here D is the data (or design) matrix based on the n data points: $D = [\vec{x}_1 \vec{x}_2 \dots \vec{x}_i \dots \vec{x}_n]$.

If the parameter vector is constrained so that the conic curve it represents is forced to be an ellipse:

$$b^2 - 4ac < 0, \quad (3.21)$$

we may also write

$$4ac - b^2 = 1. \quad (3.22)$$

In the matrix form, this quadratic constraint $\vec{a}^T C \vec{a} = 1$ is written as follows:

$$[a \ b \ c \ d \ e \ f] \begin{bmatrix} 0 & 0 & 2 & 0 & 0 & 0 \\ 0 & -1 & 0 & 0 & 0 & 0 \\ 2 & 0 & 0 & 0 & 0 & 0 \\ 0 & 0 & 0 & 0 & 0 & 0 \\ 0 & 0 & 0 & 0 & 0 & 0 \\ 0 & 0 & 0 & 0 & 0 & 0 \end{bmatrix} \begin{bmatrix} a \\ b \\ c \\ d \\ e \\ f \end{bmatrix} = 1. \quad (3.23)$$

Note that the distance $\delta(\vec{a})$ can be also expressed by $\delta(\vec{a}) = \|D \cdot \vec{a}\|^2$. Consequently, the minimisation of $\delta(\vec{a})$ is equivalent to:

$$\text{Minimize } \delta(\vec{a}) = \|D \cdot \vec{a}\| = \vec{a}^T \cdot D \cdot \vec{a}, \quad \text{subject to } \vec{a}^T \cdot C \cdot \vec{a} = 1. \quad (3.24)$$

As \vec{a} does not constitute a set of independent parameters, it is necessary to introduce the Lagrange multiplier λ before differentiating, so that we obtain the following system:

$$\begin{cases} D^T \cdot D \cdot \vec{a} - \lambda \cdot C \cdot \vec{a} = \vec{0}, \\ \vec{a}^T \cdot C \cdot \vec{a} = 1. \end{cases} \quad (3.25)$$

The first equation of the system is solved by considering the generalised eigenvectors of $D^T \cdot D \cdot \vec{a} = \lambda \cdot C \cdot \vec{a}$. If the couple eigenvalue λ_i , eigenvector \vec{u}_i is a solution, then it is also the case for the couple $\{\lambda_i, \mu \times \vec{u}_i\}$ for any μ which satisfies $\vec{a}^T \cdot C \cdot \vec{a} = 1$. Therefore:

$$\mu = \frac{1}{\sqrt{\vec{u}_i^T \cdot C \cdot \vec{u}_i}}. \tag{3.26}$$

Finally, the solutions of the simultaneous equations are: $\vec{\alpha}_i = \mu_i \cdot \vec{u}_i$. There are six eigenvalue-eigenvector pairs, each of them corresponding to a local minimum.

In fact, it has been proved [M. Pilu, 1996], [A. Fitzgibbon, 1999], that the minimisation of $\|D \cdot \vec{a}\|^2$ subject to $4ac - b^2 = 1$ admits one and only one solution which corresponds, of course, to an ellipse.

The algorithm is very simple:

1. Let $\{x_i, y_i\}$ be the coordinates of the n data points to be fitted.
2. Generate the design matrix:

$$D = \begin{bmatrix} x_1^2 & x_1y_1 & y_1^2 & x_1 & y_1 & 1 \\ x_2^2 & x_2y_2 & y_2^2 & x_2 & y_2 & 1 \\ \vdots & \vdots & \vdots & \vdots & \vdots & \vdots \\ x_i^2 & x_iy_i & y_i^2 & x_i & y_i & 1 \\ \vdots & \vdots & \vdots & \vdots & \vdots & \vdots \\ x_n^2 & x_ny_n & y_n^2 & x_n & y_n & 1 \end{bmatrix}.$$

3. Generate the combined matrix: $D^T \cdot D$.
4. Generate the constraint matrix:

$$C = \begin{bmatrix} 0 & 0 & 2 & 0 & 0 & 0 \\ 0 & -1 & 0 & 0 & 0 & 0 \\ 2 & 0 & 0 & 0 & 0 & 0 \\ 0 & 0 & 0 & 0 & 0 & 0 \\ 0 & 0 & 0 & 0 & 0 & 0 \\ 0 & 0 & 0 & 0 & 0 & 0 \end{bmatrix}.$$

5. Solve the generalized eigenvalue problem: $D^T \cdot D \cdot \vec{a} = \lambda \cdot C \cdot \vec{a}$, finding the only positive value: $\tilde{\lambda}$.
6. Find the corresponding eigenvector \vec{a} whose coordinates are the searched parameters of the ellipse.

Once \vec{a} is determined, it is easy to obtain the geometric parameters of the ellipse.

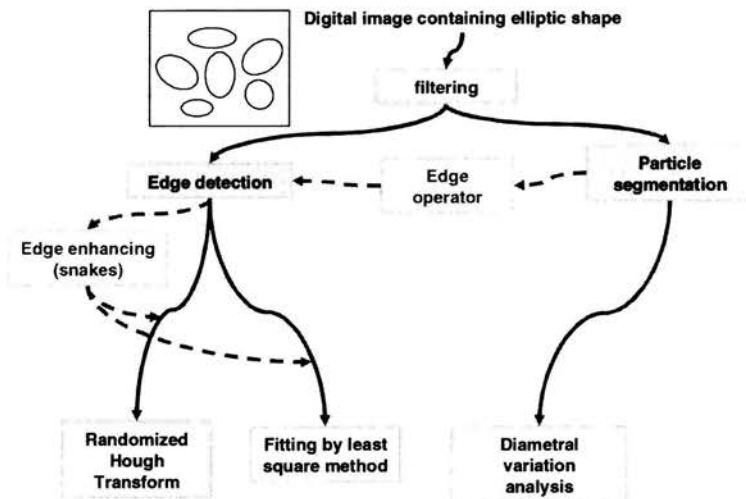


FIGURE 19.

TABLE 5.

Technique	Advantage	Disadvantage
Randomized Hough Transform	<ul style="list-style-type: none"> • Gives the parameters of the ellipses. • Can detect several elliptic edge at a time. • Works well even in case of (light) overlapping. • Ellipses do not need to be closed. • Robust towards noise and small artefacts. 	<ul style="list-style-type: none"> • Due to the randomisation, outcome can give different results if the number of set of parameters is not sufficient. • Iterative. • Somewhat slow. • It is necessary to define a lot of parameters that have an impact on the performance: the number of sets of parameters, the count threshold, the surrounding size, and so on.
Fitting by least square method	<ul style="list-style-type: none"> • Gives the parameters of the ellipses. • Ellipse does not need to be closed. • Robust towards noise and small artefacts. • Non-iterative. 	<ul style="list-style-type: none"> • One edge at a time. • Needs a great amount of memory due to the design matrix storage.
Diametrical variation analysis	<ul style="list-style-type: none"> • Gives the parameters of the ellipses but not the centre. • Somewhat fast. 	<ul style="list-style-type: none"> • One particle at a time. • Somewhat sensitive to noise (requires a good segmentation of particles).

4. Conclusion

We have presented several techniques for detecting and characterising ellipses in images. The processes can be summarised in the way depicted in Fig. 19.

Depending on the context (contrast, noise, number of particles), the three techniques that have been presented can be applied more or less successfully. Table 5 can be a useful guide in choosing either of them.

II. On Concrete Microcracking¹⁾

A. BASCOUL, M. CYR, E. RINGOT

LMDC INSA/UPS, 135 avenue de Ranguel, 31077 Toulouse, France.

5. Introduction

Even though many works about cracks and microcracks in cement based materials were published in the last years, some difficulties remain and this part of our paper aims at pointing them out and suggesting some directions for future research. For this purpose, we deal either with the relationship between the microcracked state of concrete (or mortar) and its physical properties or the characterisation of the microcracking induced under various conditions such as thermal action, shrinkage, creep or mechanical loading.

6. Means of observation

Different methods of observation are recorded in Fig. 20 according to the accuracy of the observation (indirect techniques such as acoustic emission or pulse velocity are not considered).

These means of observation are subjected to important constraints which are: artifact avoiding, nature of the material, place of measurement (in situ or experimental cores for example), easy implementation of the method, etc.

Two techniques which gives images are available: scanning electronic microscopy coupled with the replica technique and optical microscopy which are complementary according to their resolution. Both methods give bi-dimensional images avoiding bias. They can be applied to mortar or concrete. They do not require special shapes or dimensions of specimens and, finally, they can be easily carried up.

¹⁾Some part of this Section has been published already in *Concrete and Cement Composite* journal (2001).

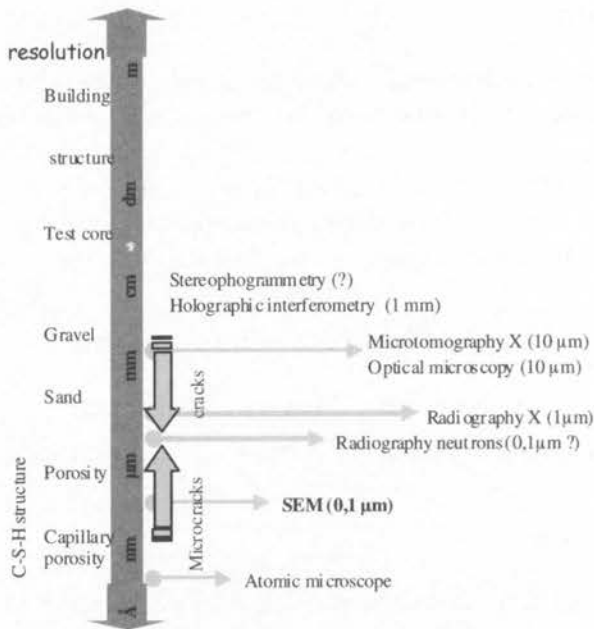


FIGURE 20. Scales covered by different methods of observation.

The replica technique as a tool for investigating microcracks in concrete was introduced by Ollivier [J.-P. Ollivier, 1985] and used extensively by several authors, cf. [E. Ringot, 1987, 1988], [V. Sicard, 1992] [A. Turatsinze, 1996]. It complies with the constraint recorded above since it allows the observer to take crack prints on surfaces of concrete without disturbing the place and the material.

Concerning optical microscopy, the reader is referred to [L.-I. Knab, 1984] [H. Hornain, 1996] who developed and enhanced methods for microcracks study in concrete. Preliminary to the observation, a dye impregnation is necessary but no drying is required thus avoiding any bias. The dye which can be in excess must be often eliminated by a slight polishing. The dye fills not only cracks but also macro-pores and porous interfacial zones.

7. Scale of observation

Most often there is a disproportion between the size of the core-test (or further more the building) and the dimensions of the images (or fields).

For example, when testing a single section of $\phi 11 \times 32$ cm cylinder, 24 images are required in optical microscopy at $G \times 10$ magnification. Each field has

a side of 2 cm which is also the dimension of one replica. If such a replica is observed within a SEM at $G \times 100$, it will be divided in 100 fields. Hence, even with low magnification, analysis of cracking requires a lot of data. Finally, image based techniques deliver data which are abundant and partial at an instant of time because of the relationship between the resolution and the studied surfaces (as shown in Fig. 21), so that one has to be careful when analysing these data.

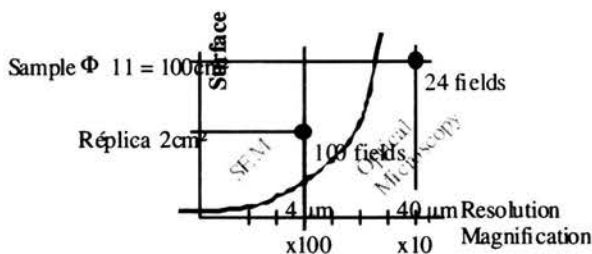


FIGURE 21. The area covered by each field increases as the square of the resolution.

8. Image analysis and crack segmentation

In the past, cracks were recognised by hand from photograph. However, attempts were performed to use image analysis in the goal of automating the process [M. Salomon, 1994], [Y. Alhassani, 1994], [A. Ammouche, 2000]. The successive steps of such a process are listed below:

1. combination of the Red-Green-Blue components into one image in the case of colour acquisition,
2. filtering: for avoiding over-segmentation,
3. binarisation,
4. shape analysis and elimination of objects which are not cracks (this stage requires the individual analysis of each component in the image and is time consuming),
5. skeletonisation.

Some remarks can be made about crack segmentation:

- Generally, most of noise filters introduce blur outlines and therefore affect boundaries of cracks.
- Most binarisation methods are based on radiometric histogram (for instance, the maximisation of entropy) More sophisticated algorithms could be applied for extracting cracks with more accuracy; among them,

for instance, classification algorithms, growing form algorithms, watershed. The employed techniques always give a positive result whatever cracks are present or not on the images so that the algorithm must be completed by a decision stage.

- Objects different from cracks can be also extracted like granulates, hydrates, fibres and so on which makes possible to reconstitute the context of cracking.
- Systematic skeletonisation forbids crack aperture analysis. In fact, most of the techniques of preparation of samples do not give accurate image of the aperture.

9. 2D crack network parameters

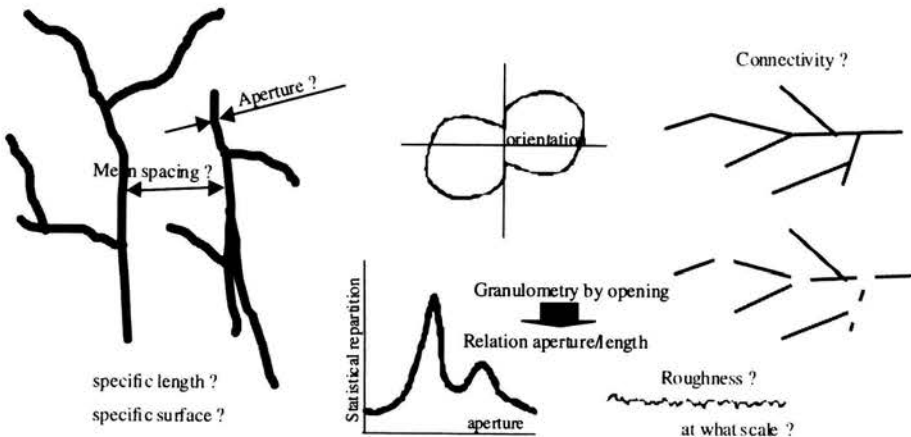


FIGURE 22. Some parameters in the plane of observation.

The specific length L_A , the intercepts $N_L(\theta)$ – or the diametrical variation – and the degree of orientation ω are often used to characterise microcrack networks.

These stereological parameters must be in accordance with the Adwiger laws [M. Coster, 1989]. For example, the parameter L_A , most often named “crack density” by the authors, depends on the magnification at which the observations have been made. As $W(\lambda L_2) \neq \lambda^2 W(L_2)$, the quantity L_2 (from which L_A is derived) is not scale homogeneous. This phenomenon is reported by Ammouche et al. in [A. Ammouche, 2000], but the authors minimise it (the magnifications they use varies only between $G \times 25$ and $G \times 80$). Small details of cracks disappear when magnification decreases since a sufficient resolution is needed to visualise the thinnest cracks. The full exploitation of

this simple statement could lead to information on the aperture of cracks. Magnification plays the role of sieve and thus it could be possible to generate something like a kind of “granulometry” of cracks.

Another point must be underlined concerning how the microcrack network covers the observed surface. For instance, it can be distributed in a non-uniform manner, so that “holes” appear at all scales. Figure 23 schematically shows such a pattern like a Sierpinski carpet. A fractal dimension can be computed from measurements at different scales as described by Mandelbrot in [B. Mandelbrot, 1983].

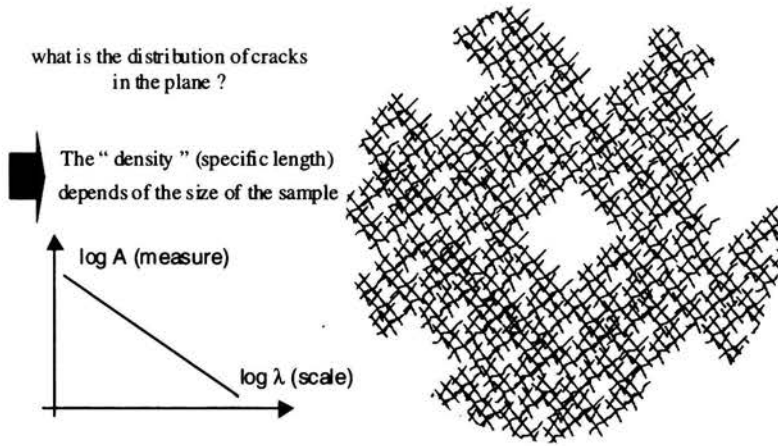


FIGURE 23. Cracks can have non-uniform density.

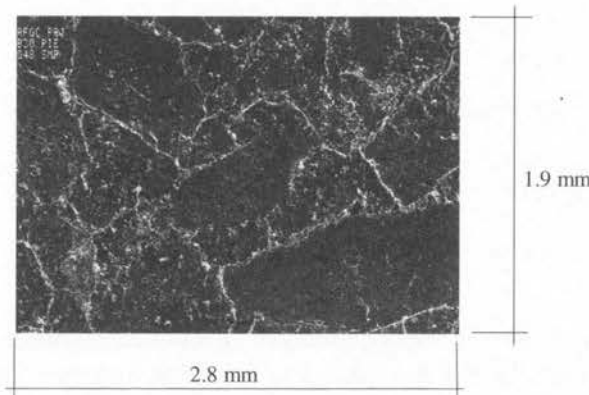


FIGURE 24. SEM replica area.

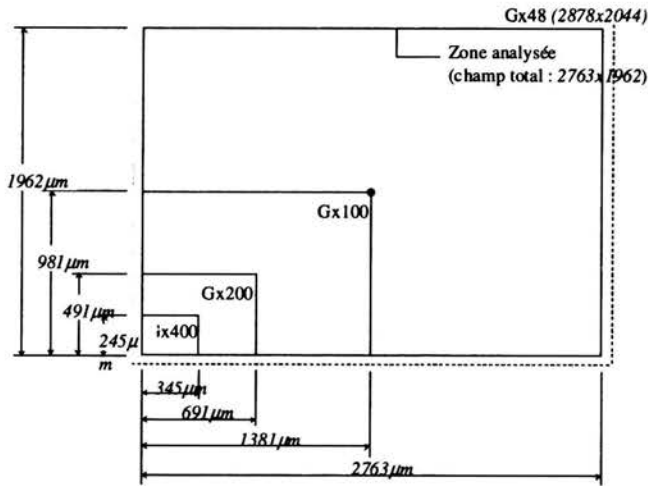


FIGURE 25. Different field sizes.

As an illustration of this point, let us have a look at a study performed with SEM. The same area of concrete (Fig. 24) has been analysed at different magnifications, thus different resolutions have been used (Fig. 25).

(a) Reconstituted crack map from 16 fields.

(b) Results from intercept analysis.

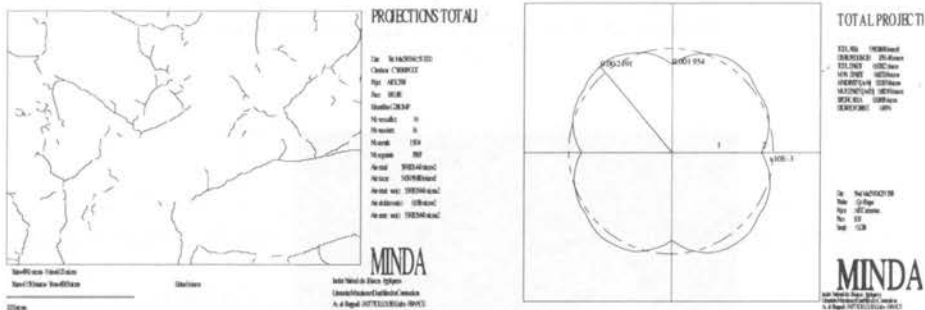


FIGURE 26. Example of analysis for G×200 magnification.

The specific length is scale dependent. Figure 27 shows how the specific length L_A varies with the field size λ in a log-log diagram. Every change in scale (in the range G×48 to G×400) verifies the equation: $L_A(\lambda) \propto \lambda^{-\alpha}$, where $\alpha = 1 - d_f$, and d_f is the homothetic dimension (or fractal dimension) of the microcracking. Here, it has been found that $d_f = 1.184$.

TABLE 6. Results for all the scales.

G×	Resolution f_v μm	Field height η μm	Analysed area A mm^2	Total length L_2 mm	Specific length L_A mm/mm^2	Specific area S_V mm/mm^2	Degree of orientation ω %
×48	3.99	2043	5.859	15.714	2.682	3.413	18
×100	1.92	983	5.399	17.728	3.283	4.178	17
×200	0.96	492	5.399	19.556	3.622	4.609	15
×400	0.48	246	5.399	23.433	4.340	5.523	13

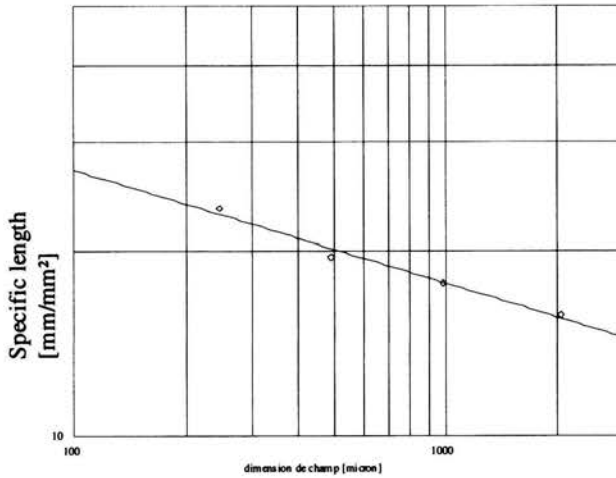


FIGURE 27. Specific length versus scale.

Attention must be paid to the roughness of the crack pattern. Several techniques based on image analysis were proposed to determine another aspect of the fractal dimension due to the roughness. Among them, Richardson's method of compass, Minkowski's method of dilation, the method of the boxes and the method of density-correlation are reported in the following references [M. Coster, 1989], [B. Mandelbrot, 1983], [K. Sandau, 1996], [J. Teixeira, 1985], and summarised in [Y. Al Hasanni, 1998].

Finally it has to be noticed that efforts must be made to characterise aperture and other parameters in relation to transport properties of the material. For example, B. Gerard and J. Marchand [A. Ammouch, 2000] proposed a

predictive model of the diffusion properties of concrete based on two parameters: the crack density and the mean effective crack aperture L_4 . However, it appears that their model needs also a tortuosity parameter (τ) and is based on the hypothesis of the continuity of the crack pattern. This interesting work shows clearly the direction for future researches on crack pattern: roughness, aperture, spacing and connectivity must be accurately quantified.

10. 3D crack network parameters

Plane observation gives a partial characterisation of the state of micro-cracking of concrete. So, it is necessary to extend the results to the three-dimensional space. The alternative ways are described in Fig. 28.

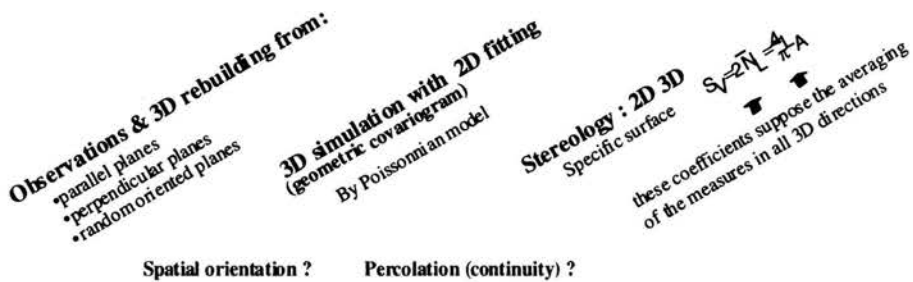


FIGURE 28. How to obtain quantitative parameters in 3D space.

Reconstruction of the spatial crack pattern from observations made in different planes would be the most accurate way for obtaining three-dimensional data. This technique is similar to tomography used in medical science, provided that the planes are parallel. Unfortunately, this approach is not realistic in materials science because it requires an enormous collection of data [J.-P. Tricart].

In fact, in most of actual situations, 2D results are extended to 3D-space by applying stereological laws restricted to the crack density. For example, assuming the isotropy of the crack pattern in all the 3D directions, the specific surface of cracks is derived from its density by the formula $S_V = \frac{4}{\pi} L_A$. This last hypothesis is not always checked because of lack of study on various oriented planes. In fact, when there is a privileged direction due to geometry of the sample and the direction of the loading, this stereological relation is not adequate.

3D simulation could be a consistent way enabling to give accurate results and realistic geometries with a reasonable amount of data. Boolean mod-

els, introduced by Jeulin [D. Jeulin, 1979], have been successfully used by Quenec'h et al. [J.-L. Quenec'h, 1993] or Ringot and Cros [E. Ringot, 1996] for describing the structure of materials.

11. Conclusion

Characterisation of cracking and microcracking in relation with the material properties still poses problem. However, image analysis and recent technological improvements in acquisition and processing, encourage more systematic and more accurate measurements. Additionally further works have to be done, particularly in order to develop methods for determining objective aperture distribution of cracks, to make multi-scale studies for determining how cracks occupy the space and finally to establish statistical models of the crack pattern. This is the price to be paid to reach quantitative correlation between the spatial crack pattern and the mechanical and physical properties of concrete.

III. On Surface of Concrete

G. LEMAIRE^{1,2)}, G. ESCADEILLAS¹⁾, E. RINGOT¹⁾

¹⁾*LMDC INSA/UPS, 135 avenue de Rangueil, 31077 Toulouse, France*

²⁾*GTM-Construction, 61 avenue Jules Quentin, 92000 Nanterre, France*

12. Introduction

In construction field, architects and building owners often request about the quality of the concrete surface [Ménard, 1999]. These requests mainly concern flatness, tint and presence of surface bubbles. In France, specifications are given with reference to an AFNOR standard [AFNOR, 1989]. Although the examination of flatness generally will not pose a problem at the building site, this is not the case for the tint and the quantity of bubbles. These last two issues often constitute a subject of conflict between owners, architects and building firm. Here we present an evaluation tool based on image analysis. The images are preliminarily corrected to take into account the light and the nature of the camera.

The analysis enables professionals to use the standard in a more objective way and it gives laboratories new qualification possibilities for evaluation of concrete surface. The originality of the method lies more in the industrial application than the complexity of the image analysis procedures.

In this Section two aspects of qualifying concrete surfaces are discussed: the colour factor and the surface bubble parameter.

13. Colour analysis

13.1. Imaging and correction

The images of concrete surfaces are produced by a digital camera under natural ambient light. Of course, the colour distribution in the raw image depends on the type of camera as well as on the incident light intensity. So, a comparison of images of the same surface but taken under various light intensities or with different cameras is not accurate. Images require an adjustment to take into account ambient conditions and camera characteristics. A process was developed to allow it [Lemaire and al., 2001]. The first step transforms the own colour camera code in a universal system as CIE Lab. The second step modifies the image to simulate the condition of a standard illuminate (D65) defined by the CIE [colorimetry, 1986].

The corrections require additional measurements on the site such as reflectance curves of concrete surface and the colour temperature of ambient light [Lemaire et al., 2001]. For these purposes, a colorimeter which gives reflectance properties and a light meter which gives illuminate characteristics [Minolta, 1994] are used.

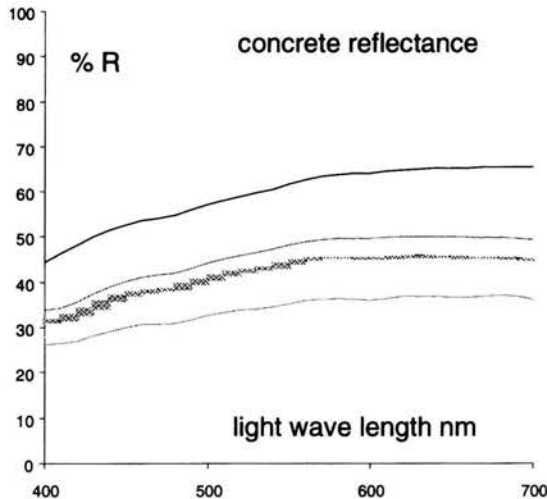


FIGURE 29. Typical curves of reflectance of a same concrete surface but at different places.

After deduction of the light spectral curve, three images, corresponding to the three colour components, i.e. luminance (L^*), tint (h^*) and saturation (C^*) [Trouvé, 1991], are computed from each photograph. It is important to note that the tint and the saturation are in a narrow range for the same concrete surface (Fig. 29). Only the luminance appears to be a significant signal.

13.2. Exploitation of luminance levels images

Architects are interested in the conformity of the surfaces with reference to their initial specifications. If needed, defaults can be analysed by a characterisation in terms of area, shape and luminance.

Obviously, the pertinent size of the smallest defaults that must be taken into account, in this evaluating work depends on the observation distance of the concrete surface. So, it is useful to introduce the notion of elementary area that can regroup several pixels on the digital image. As an example, it is not relevant to analyse details smaller than one square centimetre for a surface distant of more than fifty metres.

Among all quantitative parameters, the luminance histogram is the first tool in the evaluation of the surface quality. It gives with the medium luminance, the extreme values like an indication of the surface homogeneity. For example, the presence of several modes in the histogram or a strong spreading of the curve can reveal heterogeneity (Fig. 30).

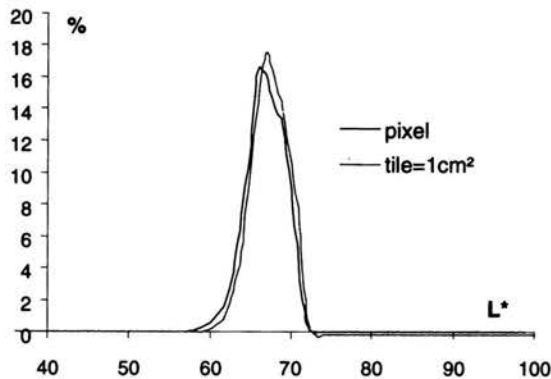


FIGURE 30. Unimodal histograms computed with two different sizes of the elementary tile.

A computer program has been created for the needs of this project. The user can choose the luminance level range that suits to him concerning the building contract requirements.

The program focuses on the areas belonging to the defined range. Every area out of the range, a surface defect, can be analysed to obtain its size, its average luminance and every other statistics parameters. As example, an image of the surface of the bridge wall is selected (Fig. 31).

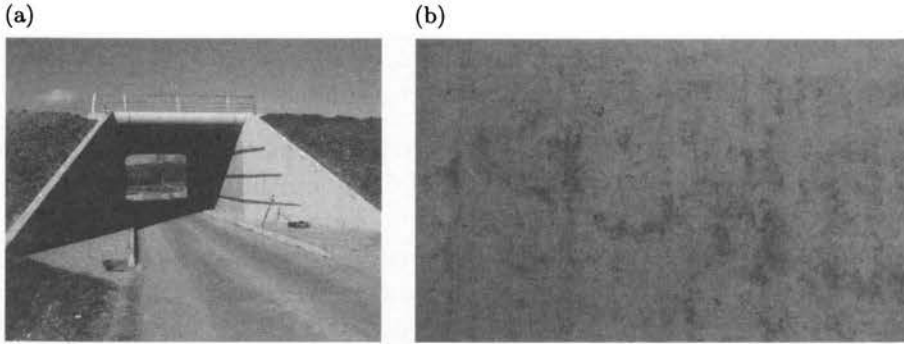


FIGURE 31. (a) Studied bridge. (b) Photograph of the surface (part).

The histogram analyses (Fig. 30) claims that 98% of the surface is located between the 62 and 72 luminance levels.

The French NF P18-503 standard [AFNOR, 1989] specifies the concrete tint classes and gives a reference of seven grey levels equivalent to a luminance scale (Fig. 32). In our example, the surface could be automatically classified in the 3rd and 4th classes by our program.

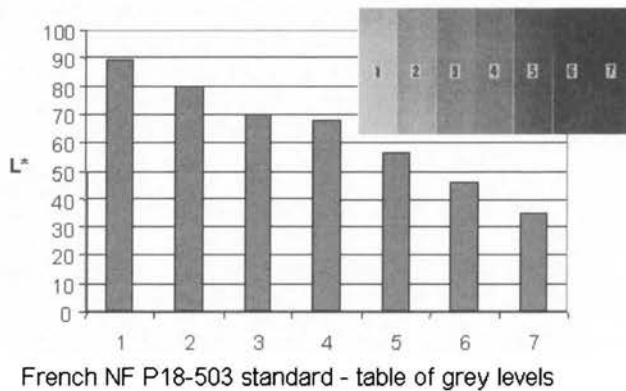


FIGURE 32. Grey classes of the standard NFP 18-503 and corresponding luminances.

The localisation of each “default” can be visualised in a false colour image (Fig. 33). Here the global default areas cover 19% of the surface.

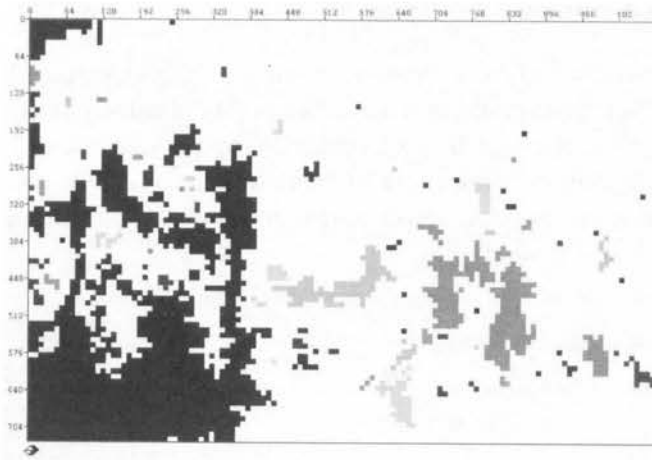


FIGURE 33. False colour image of the defaults.

Table 7 summarises luminance and area of each default larger than three square centimetres for a given surface of concrete.

TABLE 7. Statistic analysis of defaults of a surface (only the areas larger than 3 cm² were taken into account); elementary tile = 1 cm², $L^* < 65$.

No.	area [cm ²]	$L_{average}$	L_{min}	L_{max}	No.	area [cm ²]	$L_{average}$	L_{min}	L_{max}
1	44	63	61	4	16	4	64	64	64
2	4	63	63	64	17	5	63	63	64
3	5	63	63	64	18	5	62	56	64
4	5	63	63	64	19	86	62	59	64
5	4	62	62	63	20	81	62	60	64
6	22	62	59	64	21	7	64	64	64
7	15	63	62	64	22	5	63	63	64
8	6	63	63	64	23	105	62	59	64
9	6	64	64	64	24	5	62	60	65
10	1270	63	57	66	25	26	63	61	64
11	13	62	61	64	26	8	63	61	64
12	5	63	63	64	27	16	62	60	64
13	8	63	63	64	28	7	63	63	64
14	7	64	64	64	29	4	63	63	64
15	8	63	62	64	30	16	63	62	64

14. Surface bubbles analysis

French standard gives a reference scale to analyse surface bubbles (see Fig. 34). A classification of the surface is roughly obtained by comparing the bubbles on the surface with the bubbles of the reference scale. In fact, one surface can regroup several types of bubbles, so the use of the standard is difficult and subjective. A better and a more objective evaluation can be obtained with image analysis.

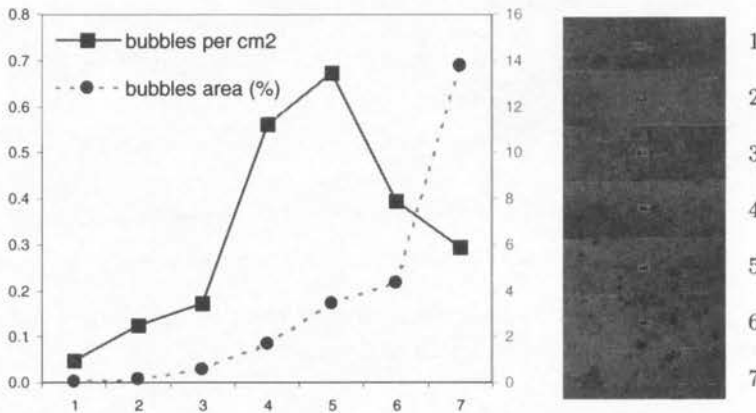


FIGURE 34. Bubbles distribution (NF P18-305) and its characteristics measured by image analysis.

The picture used to analyse surface bubbles must be taken close enough to distinguish details about one square millimetre. A ruler put on the surface analysed can give the ratio pixel/cm² is known and thus the bubbles size.

TABLE 8. Algorithm of segmentation and analysis of bubbles.

1. Median threshold: the image is filtered by a median filter in order to eliminate the noise.
2. Binary process by maximum entropy: this method detects rare objects on the image; thus it is suitable to extract bubbles from the surface images.
3. Morphologic "opening" allowing to eliminate the objects of irrelevant size.
4. Convex filter: this filter allows to complete the global geometry of the biggest bubbles which couldn't be entirely detected because of the incident light.
5. Counting and granulometry of bubbles.

The digital image is processed in the way presented in Table 8. The method is illustrated by the next example (Fig. 35). The global area covered by bubbles is 3.0%. There are 300 bubbles per square metre.

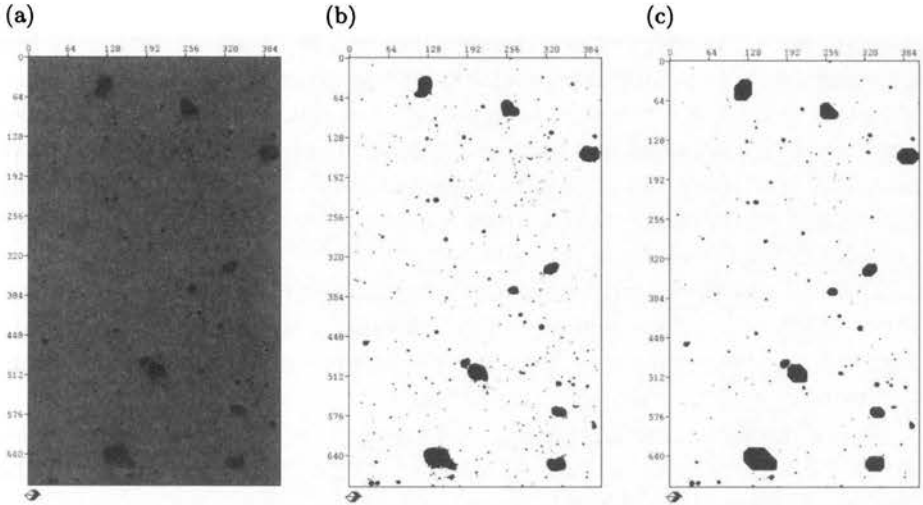


FIGURE 35. (a) Filtered image. (b) Binarisation. (c) Convex hull.

The bubble granulometry is realised by successive morphological openings (Fig. 36).

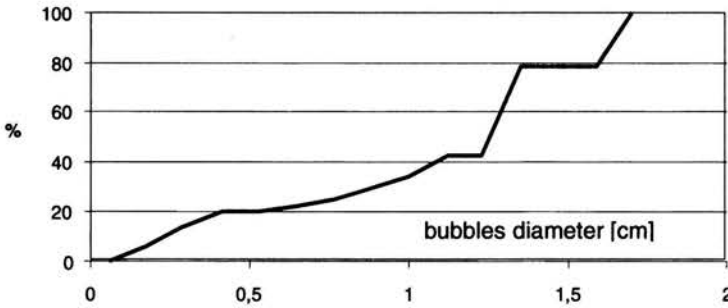


FIGURE 36. Granulometric curve of bubbles.

The method of analysis can be applied to the reference bubbles scale given by the AFNOR Table to classify concrete surfaces according to this standard. In this way, the given surface will be represented at the border of the 4th and 5th classes.

15. Discussion

Civil engineers expect tools for the characterisation of concrete surfaces with respect to their properties in terms of tint and bubbles. The standards, when they exist, propose references in term of levels of grey and bubbles quantity, but their effective use is subjective and too rudimentary. Very few documents on this subject are available for the experts.

In this context, a method for a quantitative evaluation of concrete surfaces based on image analysis has been presented. In reference to the normative texts, the developed tool allows an objective evaluation of grey levels of the surface and an accurate measurement of the area covered by bubbles. Of course, a richer information is available.

The method presented opens new perspective for civil engineering research: study of the evolution of surfaces at various ages, constitution of data bases, correlation with the influencing parameters such as the formulation, conditions of molding, climatic factors, etc.

Today the technique is already used on some building site for expertise and in laboratory with an aim of improving the control of quality of the surfaces of concrete [GTM, 2001].

References

1. AFNOR, norme NF-P18 503, surfaces et parements de béton éléments d'identification, French Standard, 1989.
2. AL HASSANI Y., BASCOUL A., RINGOT E., Microcrack study of cement-based materials by means of image analysis, *Material Research Society*, Vol.370, pp.43-48, 1994.
3. AL HASSANI Y., *Contribution à la reconnaissance de la fissuration dans le béton par analyse d'images*, Ph.D.Thesis LMDC Toulouse, 1998.
4. AMMOUCHE A., BREYSSE D., HORNAIN H., DIDRY O., MARCHAND J., A new image analysis technique for the quantitative assessment of microcracks in cement-based materials, *Cement and Concrete Research*, Vol.30, pp.25-35, 2000.
5. AMINI A.A., TEHRANI S., WEYMOUTH T.E., Using dynamic programming for minimizing the energy of active contours in the presence of hard constraints, *Proceedings of the Second International Conference on Computer Vision*, pp.95-99, 1988.
6. BRESENHAM J.E., A linear algorithm for incremental digital display of circular arcs, *ACM*, Vol.20, No.2, pp.100-106, 1977.
7. BRESENHAM J.E., Algorithm for circle arc generation, fundamental algorithms for computer graphics, *NATO ASI series*, Vol.F17, Springer Verlag, Berlin, pp.197-208, 1985.
8. CANNY J.F., A computational approach to edge detection, *IEEE Trans. Pattern Analysis and Machine Intelligence*, Vol.1, No.8, pp.679-698, 1986.
9. *Colorimetry*, (2nd ed.), CIE, 1986.

10. COSTER M., CHERMANT L.-L., *Précis d'analyse d'images*, Presses du CNRS, pp.20-23, 1989.
11. DAVIES E.R., Image space transform for detecting straight edges in industrial images, *Pattern Recognition Letters*, No.4, pp.185-192, 1986
12. DIDAY E., LEMAIRE J., POUGET J., TESTU F., *Eléments d'analyse de données*, Dunod, Paris, 1982.
13. EBERLY D., *Integer-based Algorithm for Drawing Ellipses*, 2000.
www.magix-software.com
14. FITZGIBBON A., PILU M., FISHER R.F., Direct least square fitting of ellipses, *Tern Analysis and Machine Intelligence*, Vol.21, No.5, pp.476-480, May 1999.
15. GANDER W., GOLUB G.H., STREBEL R., Least-square fitting of circles and ellipses, *BIT*, No.43, pp.558-578, 1994.
16. GÉRARD B., MARCHAND J., Influence of cracking on the diffusion properties of cement-based materials. Part I: Influence of continuous cracks on the steady-state regime, *Cement and Concrete Research*, Vol.30, pp.37-435, 2000.
17. *GTM-Construction*, brevet FR0102900, analyse chromatographique d'un parement, 2001.
18. HARALICK R., SHAPIRO L., *Computer and Robot Vision*, Addison-Wesley, 1992.
19. HORNAIN H., MARCHAND J., AMMOUCHE A., MORANVILLE M., Microscopic observation of cracks in concrete – A new sample preparation technique using dye impregnation, *Cement and Concrete Research*, Vol.26, pp.869-881, 1996.
20. HOUGH P.V.C., *Machine Analysis of Bubble Chamber Pictures*, *International Conference on High Energy Accelerators and Instrumentation*, CERN, 1959.
21. JEULIN D., *Ph.D.thesis*, Ecole Supérieure des Mines de Paris, 1979.
22. KANATANI K., Statistical bias of conic fitting and renormalization, *IEEE Trans. Pattern Analysis and Machine Intelligence*, Vol.16, No.3, pp.320-326, 1994.
23. KASS M., WITKIN A., TERZOPOULOS D., Snakes: active contour models, *Proc. of First International Conference on Computer Vision*, pp.259-269, 1987.
24. KNAB L.I., WALKER H.N., CLIFTON J.R., FULER E.R., Fluorescent thin section to observe the fracture zone in mortar, *Cement and Concrete Research*, Vol.14, pp.339-344, 1984.
25. LEAVERS V.F., *Shape Detection in Computer Vision Using the Hough Transform*, Springer-Verlag, Berlin, 1992.
26. LEMAIRE G., RINGOT E., CUSSIGH F., Colorimétrie des parements de béton, *Colloque VIM2001, Visualisation Image Modélisation*, Nancy, France, May 15th-17th, 2001.
27. MACLAUGHLIN, *Technical Report – Randomized Hough Transform: Improved Ellipse Detection with Comparison*, Technical Report No.1-1997, The University of Western Australia, Centre for intelligent information processing systems, dept of E.E.Eng., U.W.A., Stirling Hwy, Nedlands W.A.6907, Australia, 1997.
28. MANDELBROT B., *Les objets fractals*, Flammarion, (2nd ed.), 1983.

29. MARR D., HILDRETH E., Theory of edge detection, *Proceeding of the Royal Society London*, Vol.B207, pp.187-217, 1980.
30. MÉNARD J.-P., La qualité pour tous les usages, *Constructions Moderne*, No.101, p12, 1999.
31. Minolta, *Analyse des couleurs, parlons clair*, Document Minolta, 49pp., 1994.
32. OLLIVIER J.-P., A non destructive procedure to observe microcracks of concrete by scanning electron microscope, *Cement and Concrete Research*, Vol.15, pp.1055-1060, 1985.
33. PAVLIDIS T., Algorithms for graphics and image processing, *Computer Science Press*, Rockville, 1982.
34. PILU M., *Part-based Grouping and Recognition: a Model-guided Approach*, Dept. Artificial Intelligence, Univ. of Edinburgh, PhD thesis, August 1996.
35. PORRILL J., Fitting ellipses and predicting confidence envelopes using a bias corrected Kalman filter, *Image and Vision Computing*, Vol.8, No.1, pp.37-41, October 1993.
36. QUENEC'H J.-L., COSTER M., CHERMANT J.-L., Application of probabilistic models to the description of the growth of titanium carbides during liquid phase sintering, *Acta Stereologica*, Vol.13, pp.287-292, 1993.
37. ROSIN P.L., A note on the least square fitting of ellipse, *Pattern Recognition Letters*, No.14, pp.799-808, October 1993.
38. RINGOT E., OLLIVIER J.-P., MASO J.-C., Characterisation of initial state of concrete with regard to microcracking, *Cement and Concrete Research*, Vol.17, pp.411-419, 1987.
39. RINGOT E., Development of the map cracking in concrete under compressive loading, *Cement and Concrete Research*, Vol.18, pp.933-942, 1988.
40. RINGOT E., CROS H., *Boolean Model of the Fresh Cement Paste Structure*, Réunion du réseau GEO, Aussois France, 1996.
41. SALOMON M., PANETIER M., Quantification du degré d'avancement de l'alkali-réaction dans les bétons et la microfissuration associée, *Proc. of 3rd Cannet/Aci, International Conference on Durability of Concrete, Nice*, pp.383-401, 1994.
42. SAMPSON P.D., Fitting conic sections to very scattered data: an iterative refinement of the Bookstein algorithm, *Computer Graphics and Image Processing*, No.18, pp.97-108, 1982.
43. SANDAU K., A further method to measure fractal dimension and the maximum property, *Acta Stereologica*, Vol.15/1, pp.83-90, 1996.
44. SCHULER A., *The Randomized Hough Transform Used for Ellipse Detection*, paper found on Internet, 2001.
45. SICARD V., FRANÇOIS R., RINGOT E. PONS G., Influence of creep and shrinkage on cracking in high strength concrete, *Cement and Concrete Research*, Vol.22, pp.159-168, 1992.
46. TAUBIN G., Estimation of planar curves, surfaces and non planar spac curves defined by implicit equation, with application to edge and range image segmentation, *IEEE Trans. Pattern Analysis and Machine Intelligence*, Vol.13, No.11, pp.1115-1138, November 1991.

47. TEIXEIRA J., Experimental methods for studying fractal agregates. On growth and form, *NATO ASI, Series E: Applied Sciences*, No.100, Cargèse, Corsica, France, 1985.
48. TRICART J.-P., BREVART O., BARANGER R., MARTINEZ L., Analyse quantitative d'images électroniques et chimiques, *Bulletin des Centres de Recherche Elf-Aquitaine*, Vol.15, pp.279-305, 1991.
49. TROUVÉ A., *La mesure de la couleur*, AFNOR CETIM, 1991.
50. TURATSINZE A., BASCOUL A., Restrained crack widening in mode I crack propagation for mortar and concrete, *Advanced Cement Based Materials*, Vol.4, pp.77-92, 1996.
51. WILLIAMS D.J., SHAH M., Edge contours using multiple scales, *Computer Vision Graphics Image Processing*, No.51, pp.256-274, 1990.
52. WILLIAMS D.J., SHAH M., A fast algorithm for active and curvature estimation, *Image Understanding*, Vol.55, No.1, pp.14-26, 1992.
53. WU W., WANG M.J., Elliptical object detection by using its geometrical properties, *Pattern Recognition*, No.28, pp.117-124, 1995.

